In situ synthesis of bowl-shaped TiO_2/C from MXene heat treatment for photocatalytic CO_2 reduction

YU Hao, LI Yuling, HU Zhihui, LI Qin*

(Key Laboratory of Catalysis and Energy Materials Chemistry of Ministry of Education & Hubei Key Laboratory of Catalysis and Materials Seience, South-Central Minzu University, Wuhan 430074, China)

Abstract The *in situ* synthesis of TiO_2 semiconductor photocatalysts using Ti_3C_2 MXene materials offers a highly effective approach to mitigate environmental and energy challenges by selectively reducing CO_2 to valuable chemicals like CH_4. However, the transformation of Ti_3C_2 into TiO_2 is usually accompanied by severe agglomeration of particles, which leads to a reduction in the number of intrinsic active sites, adversely affecting the adsorption and conversion of CO_2. To address this problem, polymethyl methacrylate (PMMA) was employed as a hard template to fabricate a bowl-shaped TiO_2 supported on carbon layer (TiO_2/C) hybrid photocatalyst by a calcination method. The results showed that the obtained sample had a sufficiently large specific surface area and numerous active sites for CO_2 adsorption and activation. The excellent conductivity of the carbon layer facilitated the separation of photogenerated carriers produced by TiO_2, enabling the obtained TiO_2/C complexes exhibit CO_2 reduction rates to CO and CH_4 of 1.84 $\mu mol \cdot g^{-1} \cdot h^{-1}$ and 5.32 $\mu mol \cdot g^{-1} \cdot h^{-1}$, respectively, with the CH_4 selectivity of 74%. The precise utilization of templates to refine the morphology of MXene oxidation products was thus demostrated, offering a practical approach for the application of MXene in the photocatalysis.

Keywords photocatalytic; CO_2 reduction; TiO_2; Ti_3C_2 MXene; CH_4

中图分类号 O64 **文献标志码** A **文章编号** 1672-4321(2026)02-0277-12

doi:10.20056/j.cnki.ZNMDZK.20250846

MXene热处理原位制备碗状TiO_2/C及其光催化CO_2还原性能研究

于浩,李玉玲,胡志慧,李覃*

(中南民族大学 催化转化与能源材料化学教育部重点实验室暨湖北省催化材料科学重点实验室,武汉 430074)

摘 要 使用Ti_3C_2 MXene材料原位合成TiO_2半导体光催化剂,通过将CO_2选择性还原为CH_4等有价值的化学物质,为缓解环境和能源挑战提供了一种非常有效的方法.然而,Ti_3C_2转化为TiO_2的过程中通常伴随着严重的颗粒团聚,这导致固有活性位点数量减少,对CO_2的吸附和转化产生不利影响.为了解决这个问题,使用聚甲基丙烯酸甲酯(PMMA)作为硬模板,通过煅烧法制备了碗状碳层负载TiO_2(TiO_2/C)混合光催化剂.结果表明:所得样品具有足够大的比表面积和丰富的CO_2吸附和活化位点.此外,碳层的优异导电性有利于TiO_2产生的光生载流子的分离.所得TiO_2/C复合物的CO_2还原为CO和CH_4的速率分别为1.84 $\mu mol \cdot g^{-1} \cdot h^{-1}$和5.32 $\mu mol \cdot g^{-1} \cdot h^{-1}$,$CH_4$选择性为74%.该工作展示了利用模板精确控制MXene氧化产物形貌的方法,为MXene在光催化的应用提供了一种切实可行的实践方案.

关键词 光催化;二氧化碳还原;二氧化钛;碳化钛;甲烷

Photocatalytic technology has garnered increasing attention due to its potential to address the energy crisis and global warming stemming from the extensive consumption of fossil fuels[1-3]. Among various photocatalytic reactions, photocatalytic CO_2 reduction technology holds significant promise. It can mitigate the greenhouse effect while converting CO_2 into valuable chemicals and fuels, such as carbon monoxide (CO) and methane (CH_4)[4-5]. Among the reduction products, CH_4 is particularly advantageous owing to its high

收稿日期 2025-05-15

* **通信作者** 李覃(1987-),女,副教授,博士,研究方向:光催化,E-mail: liqin0518@mail.scuec.edu.cn

基金项目 国家自然科学基金资助项目(21972171)

energy density and the carbon-neutral nature of its combustion byproducts[6]. Over the past few years, semiconductor materials like TiO_2[7], CdS[8], g-C_3N_4[9], BiOBr[10], and In_2O_3[11] have been extensively investigated for photocatalytic CO_2 reduction. Among these, TiO_2 has emerged as a popular candidate material, thanks to its suitable band structure, excellent chemical stability, environmental and biological compatibility, and low cost[12-14]. However, the catalytic performance and selectivity of bare TiO_2 nanomaterials for photocatalytic CO_2 conversion into CH_4 are significantly hindered by their weak light absorption and rapid recombination of photogenerated carriers.

To address the aforementioned issues, various strategies have been proposed to enhance the photocatalytic performance of TiO_2, such as morphology regulation[15], elemental doping[16], heterojunction construction[17] and cocatalysts loading[18]. In particular, the combination of TiO_2 with cocatalysts can significantly improve its ability to capture photogenerated electrons, thereby promoting the migration and separation of photogenerated carriers and enhancing its catalytic efficiency for CO_2 conversion[19-20]. In recent years, carbon materials have garnered significant attention as ideal cocatalysts due to their excellent chemical stability, tunable surface properties, and large specific surface area[21-22]. However, conventional methods for preparing C-doped TiO_2 materials typically involve the use of additional carbon sources, such as polymers[23], organic solvents[24], and carbon-containing inorganic salts[25], which may introduce impurities.

As a novel two-dimensional transition metal carbide, Ti_3C_2 MXene has sparked extensive research interest since its breakthrough synthesis in 2011[26]. The atomic-scale thickness coupled with superior electronic conductivity renders it a superior co-catalyst in photoelectrochemical systems. More importantly, the surface of Ti_3C_2 MXene is rich in functional groups such as —OH and —O. These functional groups can promote the oxidation of Ti atoms. Through a self-sacrificial mechanism, they can activate the Ti—C bonds, enabling the in situ preparation of TiO_2 and the formation of a carbon layer, thereby synthesizing a binary hybrid catalyst[27]. When the C layer is coupled with TiO_2, the excellent electrical conductivity of the C layer facilitates rapid electron transfer at the interface, thereby enhancing the separation efficiency of photogenerated carriers in TiO_2[28-30].

Nevertheless, after oxidation, Ti_3C_2 tends to stack and aggregate, which severely affects the catalyst's ability to adsorb and activate CO_2 molecules, thereby limiting the CO_2 conversion efficiency. Currently, most studies report that template methods can be used to control the morphology of the catalyst to address the issue of insufficient surface active sites[31-33]. Compared with other polymers, polymethyl methacrylate (PMMA) is easier to remove, has a rich surface functional group, and has a mature production process, making it a relatively perfect template[34-37]. However, to date, there have been few reports using PMMA as a template to control the morphology of Ti_3C_2 for the preparation of TiO_2-based materials.

In this study, a combination of templating and calcination methods was employed to oxidize Ti_3C_2 and synthesize TiO_2/C composite materials. PMMA was used as a template, and its rich surface groups enabled tight bonding with Ti_3C_2, forming a PMMA/Ti_3C_2 core-shell structured compound. This structure stabilized the morphology of Ti_3C_2 during the oxidation process. Calcination not only facilitated the kinetics of Ti_3C_2 oxidation but also removed the PMMA sacrificial template, resulting in the fabrication of TiO_2/C composite materials with a bowl-like structure. This structure significantly mitigated the aggregation of TiO_2, thereby enhancing the catalytic activity and selectivity in a gas-phase CO_2 reduction system. Infrared spectroscopy revealed the key intermediate species involved in the adsorption and transformation of CO_2 on the surface of the bowl-like TiO_2/C catalyst, providing insights into the photocatalytic CO_2 reduction mechanism.

1 Materials and methods

1.1 Materials

The Ti_3AlC_2 (98%) power was acquired from Forsman Technology (Beijing) Co., Ltd. HCl (AR), LiF (AR), ethanol (AR), sodium bicarbonate

（$NaHCO_3$，AR）and sulfuric acid solution（2 mol·L^{-1}）were purchased from Sinopharm Chemical Reagent Co.，Ltd. Polymethyl methacrylate（PMMA，AR）was offered by Lianlianfa Plastics & Chemicals.

1.2　Material preparation

1.2.1　Preparation of ultrathin Ti_3C_2 nanosheets

A HF-free LiF-HCl etching strategy was employed to prepare Ti_3C_2 nanosheets. Specifically，5 g of LiF was dispersed in a polytetrafluoroethylene（PTFE）beaker containing a mixture of 25 mL deionized water and 75 mL hydrochloric acid（HCl）. Ti_3AlC_2 powder was then slowly added to the mixture. After heating at 50 ℃ for 10 h，the product was collected by vacuum filtration and subsequently dried under vacuum at 60 ℃ for 12 h. The resulting product was then added to deionized water and sonicated in an ice bath for 4 h. Finally，the Ti_3C_2 nanosheets were obtained via freeze-drying.

1.2.2　Synthesis of bowl-like TiO_2/Ti_3C_2

PMMA（0.2 g）was added to a beaker containing 50 mL deionized water and ultrasonicated for 10 min to form a homogeneous mixture. Subsequently，0.02 g of Ti_3C_2 was added and stirred for another 10 min to allow complete combination of PMMA and Ti_3C_2 through electrostatic interactions. The resulting mixture was then centrifuged at 10000 r·min^{-1} and dried at 60 ℃ for 12 h to obtain the composite named TP，where T and P represent Ti_3C_2 and PMMA，respectively.

The TP samples were placed in an air atmosphere at 450 ℃ and calcined for different durations，namely 0.5，1，3，6，9，12，and 15 h，to obtain samples designated as TP-*x*，where *x* signifies the calcination time. The synthetic process for preparing samples is illustrated in Fig. 1. For the control experiment，the same procedure was used to directly calcine Ti_3C_2 nanosheets for 9 h to obtain the T-9 sample. Additionally，the TP-9 sample was calcined at 550 ℃ for 4 h to produce the TiO_2 sample.

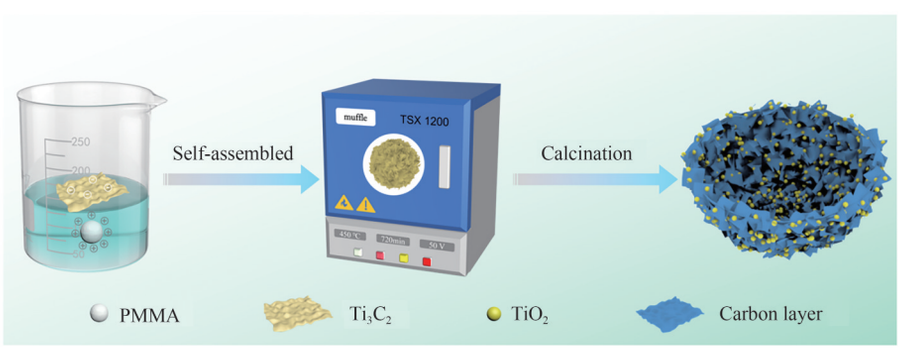

Fig. 1　Schematic diagram of the preparation process of the TiO_2/C sample.

图1　TiO_2/C样品制备流程图

1.3　Characterization

The X-ray diffraction（XRD）patterns were recorded using an X-ray diffractometer（D8 ADVANCE，Bruker）with Cu Kα radiation（λ = 1.54056 Å）at a scanning rate of 5°·min^{-1} over a 2θ range of 10° to 80°. Raman spectra were obtained using a laser confocal Raman spectrometer（Thermo Fisher Scientific，DXR 2xi）. The morphology of the samples was observed using a SU8010（Hitachi）field emission scanning electron microscope（FESEM）and a Talos F200X（Thermo Scientific）transmission electron microscope（TEM）. The composition of the samples was investigated using high-angle annular dark-field scanning/transmission electron microscopy（HAADF-STEM，Talos F200s，Thermo Scientifc）and energy-dispersive X-ray spectroscopy（EDS）. The nitrogen adsorption-desorption isotherms were recorded using a nitrogen adsorption-desorption apparatus（ASAP2020，Micromeritics）to determine the Brunauer-Emmett-Teller（BET）specific surface area（S_{BET}）of the catalysts，with degassing at 200 ℃ prior to measurement. Pore size distribution curves were derived from the adsorption isotherm data. UV-vis diffuse reflectance spectra（UV-vis DRS）were tested using a UV-vis spectrophotometer（UV2550，Shimadzu）. X-ray photoelectron spectroscopy（XPS）（Escalab 250xi，Thermo Scientific）was used to collect information on the composition and chemical

states of the samples, with all binding energies referenced to the C 1s line at 284.8 eV obtained from adventitious carbon. *In situ* diffuse reflection infrared Fourier transform spectroscopy (*In situ* DRIFTS) was conducted using a Bruker Tensor II infrared spectrometer. The C and O elemental contents of the samples were measured using a CHNS elemental analyzer (Vario EL cube) and a rapid oxygen determinator (Rapid OXY cube).

1.4 Photocatalytic activity testing

Photocatalytic CO_2 reduction activity tests were conducted in a glass automatic online gas analysis system (Labsolar-6A, Perfect Light) using a 300 W xenon lamp (PLS-SXE300, Perfect Light) to simulate sunlight. The photocatalytic activity test mainly consisted of three steps: catalyst coating, *in situ* CO_2 generation, and photocatalytic CO_2 reduction reaction. First, 30 mg of the photocatalyst was dispersed in 10 mL of deionized water to form a suspension, which was then dried to form a surface film. Second, 2.1 g of $NaHCO_3$ powder was placed at the bottom of a homemade reactor, and the coated sample was placed directly above a quartz tripod. After sealing, the air inside the reactor was evacuated. Subsequently, 20 mL sulfuric acid (2 mol·L^{-1}) was added to the reactor to react with $NaHCO_3$ and generate CO_2. Finally, the reactor was placed under the xenon lamp for 4 h. Meanwhile, the Labsolar-6A gas analysis system extracted a certain amount of gas from the reactor every hour and injected it into a GC-2014 gas chromatograph equipped with flame ionization detector (FID) and thermal conductivity detector (TCD) detectors to detect the reaction products.

1.5 Photoelectrochemical measurements

Transient photocurrent response (TPR) and electrochemical impedance spectroscopy (EIS) photoelectrochemical measurements were performed in a three-electrode system (CHI760E electrochemical workstation, Shanghai, China). The electrolyte was 0.5 mol·L^{-1} Na_2SO_4 aqueous solution, and the light source was a 365 nm LED lamp. For TPR and EIS measurements, the working electrode was prepared by coating the sample onto a 0.9 cm × 1.1 cm fluorine-doped tin oxide (FTO) glass electrode. A platinum wire and an Ag/AgCl electrode were used as the counter electrode and reference electrode, respectively. The frequency range was from 0.1 to 1000 Hz.

2 Results and Discussion

2.1 Morphological and structural analysis

The morphology and structure of the samples were analyzed using FESEM and STEM. The Ti_3C_2 prepared by the LiF-HCl etching method exhibited a monolayered sheet-like structure[38]. After being combined with PMMA, the Ti_3C_2/PMMA (TP) sample presented a core-shell structure with a wrinkled spherical morphology, with the size of the spheres being approximately 1 μm (Fig. 2(a)). As observed in Fig. 2(b)-(f), following calcination, the PMMA, which served as the "core" structure in the TP sample, began to disappear, resulting in the formation of bowl-like structures. With further increase in calcination time (>12 h), the bowl-like structures became increasingly incomplete and gradually transformed into irregular, small-sized nanosheets (Fig. 2(g)-(h)). Additionally, as shown in Fig. 2(i), direct calcination of Ti_3C_2 resulted in a multilayered sheet-like stacked structure rather than a bowl-like structure, demonstrating that PMMA played a crucial role as a template in the formation of the thin-walled bowl-like structures.

Further observations of the sample composition using STEM revealed that after calcination, Ti_3C_2 was transformed into a semi-transparent carbon layer and TiO_2 nanoparticles with a size of approximately 30 nm. Additionally, the 2D structure morphology was observed to curl up after calcination, with the surface no longer being flat (Fig. 3(a)). In contrast, the TP-9 sample, prepared by calcining Ti_3C_2 loaded on a PMMA template, maintained a 2D sheet-like structure even after the same duration of calcination (Fig. 3(h)), without undergoing the deformation seen in Fig. 3(a).

The HRTEM images of the T-9 and TP-9 samples showed a lattice spacing of 0.35 nm, confirming the presence of anatase TiO_2 (101). The absence of other lattice fringes, combined with the XRD results, confirms that the TiO_2 in both T-9 and TP-9 samples primarily exists in the anatase phase (Fig. 3(b) and (i)). The layered structure of the substrate originated from amorphous carbon rather than Ti_3C_2, thereby confirming

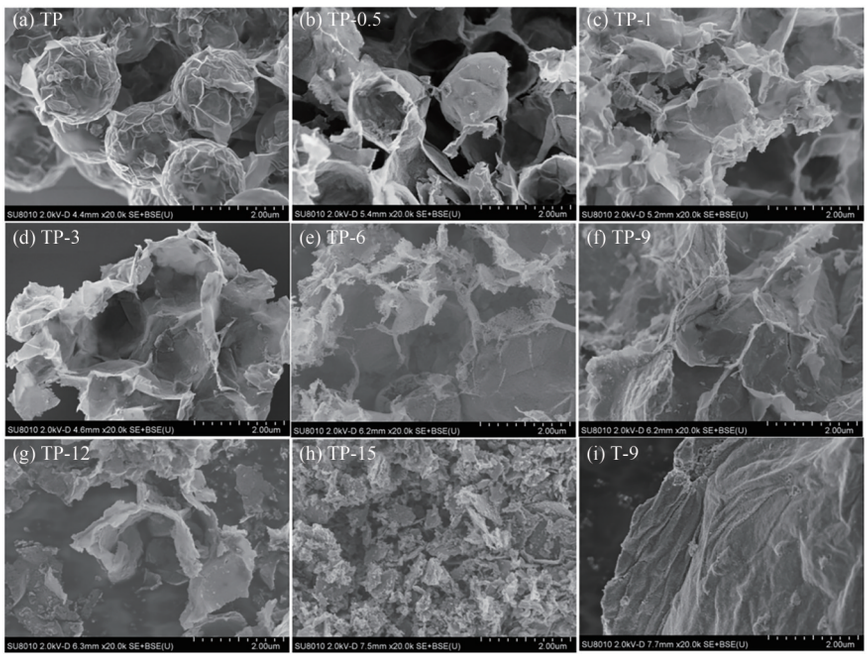

(a) TP；(b) TP-0.5；(c) TP-1；(d) TP-3；(e) TP-6；(f) TP-9；(g) TP-12；(h) TP-15；(i) T-9

Fig. 2　Morphological characterization of the materials

图2　材料的形貌表征

the successful preparation of the TiO_2/C binary composite after calcination of Ti_3C_2.

Energy-dispersive X-ray spectroscopy (EDS) analysis results (Fig. 3©-(g) and Fig. 3(j)-(n)) revealed that both the T-9 and TP-9 samples were composed of C, Ti, O, and F elements. However, the elemental content was different between the two samples. Considering that EDS exhibits data fluctuations in elemental analysis depending on the measurement location, the elemental composition of the samples was further analyzed using an elemental analyzer (for C, H, N, S) and a rapid oxygen determinator (for O). The results measured for TP-9 and T-9 in Tab. 1 showed that the mass ratio of C to TiO_2 was 0.06 in TP-9 and 0.07 in T-9, indicating of relatively lower carbon content in TP-9. This demonstrated that employing PMMA as a template not only controlled the sample's morphology and prevented the stacking of carbon nanosheets, but also promoted the oxidation of the carbon layer, thereby reducing the light-shielding effect.

The structural composition and crystalline properties of the samples were analyzed through XRD and Raman. As shown in Fig. 4(a), the prepared TP samples exhibited characteristic peaks of PMMA (2θ = 15°) and the strongest diffraction peak of the (002) plane of Ti_3C_2 (2θ = 9.1°), indicating the successful combination of Ti_3C_2 and PMMA[39]. To elucidate the mechanism behind the successful formation of PMMA/Ti_3C_2 composites, the Zeta potentials of PMMA and Ti_3C_2 were measured. The results demonstrated that PMMA and Ti_3C_2 exhibited Zeta potentials of 12.6 mV and −8.2 mV, respectively, suggesting of their opposite surface charges. This charge complementarity clearly indicated that Coulombic interactions served as the predominant binding mechanism between these components. After calcination, the characteristic diffraction peaks of PMMA and Ti_3C_2 disappeared, and the characteristic peaks of anatase TiO_2 (JCPDS card NO. 71-1167) emerged. Observing the characteristic peak of the (101) plane of anatase TiO_2 at 2θ = 25.4°, it could be seen that the peak intensity increased with prolonged calcination time, indicating enhanced oxidation of Ti_3C_2[40]. Fig. 4(b) further illustrated that with extended calcination time, the D and G band peaks of amorphous carbon in the TP-*x* samples gradually weakened, and the characteristic spectrum of TiO_2 appeared. This indicated that Ti_3C_2 was oxidized to anatase TiO_2, but the residual D and G band peaks suggested that in addition to TiO_2, the oxidation of Ti_3C_2 also

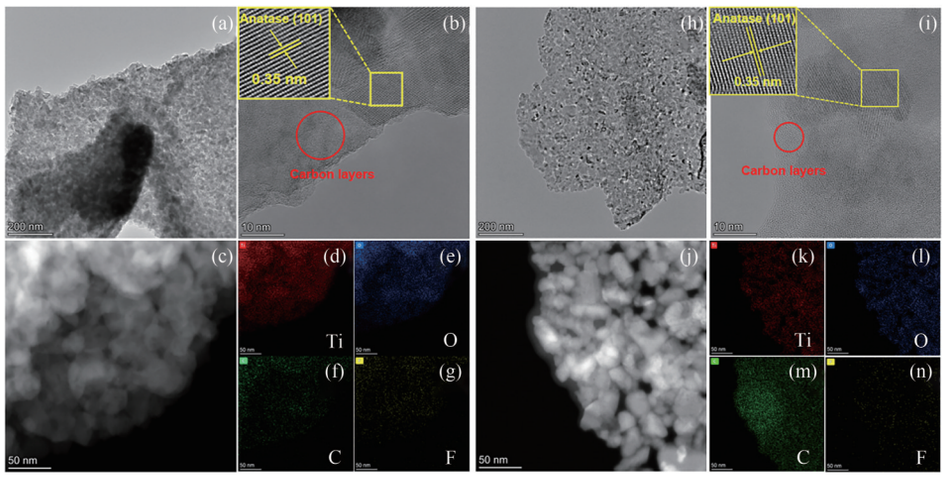

(a) TEM, (b) HRTEM, (c) HAADF-STEM and EDS mapping images of (d) Ti, (e) O, (f) C, and (g) F atoms of T-9 sample; (h) TEM, (i) HRTEM, (j) HAADF-STEM and EDS mapping images of (k) Ti, (l) O, (m) C, and (n) F atoms of TP-9 sample

Fig. 3 Morphological and element characterization of the materials.

图3 样品的形貌和元素分析表征

Tab. 1 C, O element content and the mass ratio of C to TiO_2

表1 样品C、O元素百分比含量和C与TiO_2的质量比

Sample	Atomic percent/%		$w(C):w(TiO_2)$
	C	O	
T-9	0.67	1.85	0.07
TP-9	0.92	2.80	0.06

generated a carbon layer, thereby confirming that the prepared samples were composites of the carbon layer and TiO_2. The significantly lower intensity of the amorphous carbon peak in the T-9 sample compared to the TP-9 sample indicated that the TP-9 sample had more carbon layers to facilitate the separation and transfer of carriers.

X-ray photoelectron spectroscopy (XPS) is used to characterize the chemical and electronic states of the samples for structural analysis of the substance. As observed in Fig. 5 (a), the XPS spectrum of the T sample (Ti_3C_2) exhibited characteristic peaks of F 1s and Cl 2p, which were attributed to surface groups of Ti_3C_2. However, after calcination, the TP-9 sample only showed peaks for Ti 2p, O 1s, and C 1s, which were characteristic of TiO_2 and C. The absence of F element indicateed that there was almost no residual Ti_3C_2 in the TP-9 sample. The D and G band peaks observed in Fig. 4 (b) belonged to C rather than Ti_3C_2. What is more, the high-resolution XPS spectrum of Ti 2p in Fig. 5 (b) confirmed this finding. Notably, the Ti 2p peaks of the TP-9 sample shifted to lower binding energies by approximately 0.1 eV compared to those of pure TiO_2. This shift suggested that the photogenerated holes in TiO_2 were transferred to the carbon layer[41]. Therefore, the carbon layer not only serves as a

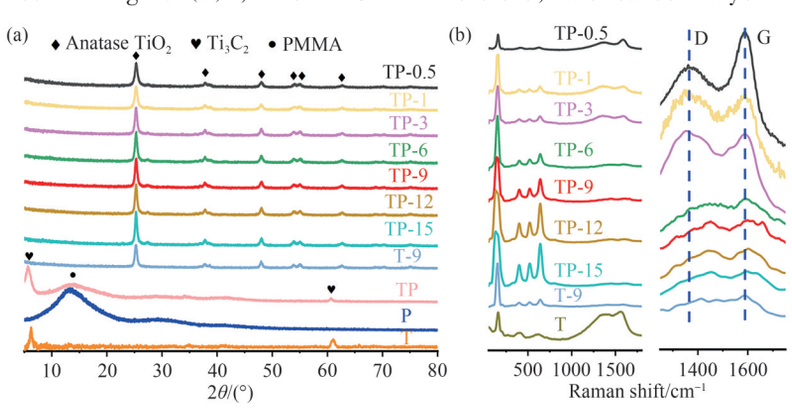

(a) XRD patterns and (b) Raman spectra of TP, TP-0.5, TP-1, TP-3, TP-6, TP-9, TP-12, TP-15, and T-9 samples

Fig. 4 Characterization of phase constituent of the materials

图4 材料的物相组分表征

carrier to enhance the light absorption properties of TiO_2 but also facilitates the separation efficiency of photogenerated electron-hole pairs, thereby improving the photocatalytic performance of TiO_2.

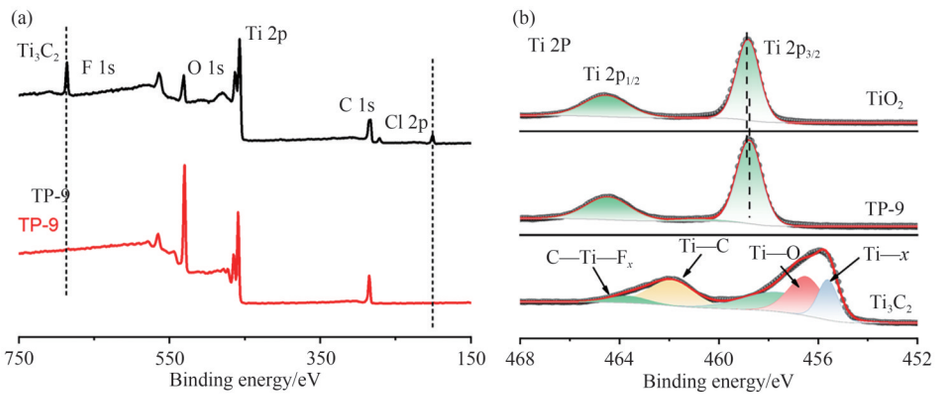

(a) XPS survey spectra of TP-9 and Ti_3C_2; (b) High-resolution spectra of Ti 2*p* in the samples

Fig. 5　Chemical state and compositional characterization of the samples

图5　样品的化学态和组成表征

2.2　Photocatalytic performance

The photocatalytic performance of the prepared samples was verified through CO_2 reduction tests. As shown in Fig. 6(a), the photocatalytic CO_2 reduction ability of the samples first increased and then decreased, exhibiting a volcano-shaped trend. Among them, the T-9 sample, obtained by directly calcining Ti_3C_2 without PMMA, had the lowest CO_2 conversion efficiency. In contrast, the TP-9 sample with a bowl-like morphology, prepared using PMMA-loaded Ti_3C_2 in the same calcination condition (450 ℃, 9 h), showed the best performance. The generation rates of CH_4 and CO from CO_2 conversion reached 1.84 and 5.32 $\mu mol \cdot g^{-1} \cdot h^{-1}$, respectively, which is about 8.5 times higher than that of the T-9 sample in terms of photocatalytic CO_2 reduction efficiency. In addition, the TP-9 sample showed a higher selectivity towards CH_4 conversion, reaching 74% (Fig. 6(b)). To verify the carbon source of the generated products, isotopic labeling experiments were conducted. As shown in Fig. 6(c) and (d), strong peak signals appeared at *m/z* = 17 and *m/z* = 29 in the reaction products, which correspond to ^{13}C-labeled $^{13}CH_4$ and ^{13}CO, respectively. This indicated that the generated CH_4 and CO mainly originated from the reduction of CO_2, rather than from the sample or other impurity carbon sources.

To verify the reason behind the enhanced CO_2 reduction performance of the samples, nitrogen adsorption-desorption isotherm tests were employed for characterization. As depicted in Fig. 7 (a), the nitrogen adsorption behavior of each sample was presented across a broad spectrum of relative pressures. All isotherms displayed typical IV characteristics, indicating the presence of a mesoporous structure within the material. Notably, in the low relative pressure region, TP-9 exhibited a significantly higher adsorption capacity compared to T-9. This was evidenced by their specific surface areas of 54.0 $cm^3 \cdot g^{-1}$ and 20.2 $cm^3 \cdot g^{-1}$, respectively. The abundant microporous structure of TP-9 was conducive to the preferential adsorption of gas molecules at low pressure. Fig. 7(b) provided insight into the specific surface activity of the sample. Here, TP-9 standed out with the highest CO and CH_4 generation rates per unit surface area, as well as the highest specific surface activity. Consequently, TP-9 demonstrates the most outstanding CO_2 reduction performance.

2.3　Photocatalytic mechanism

To explore the factors influencing the activity of the samples, their light absorption properties were characterized using UV-Vis diffuse reflectance spectroscopy. As shown in Fig. 8a, all the samples except the TP sample exhibited an absorption edge, which was consistent with that of TiO_2, indicating that the TP sample were successfully converted to TiO_2 upon calcination. With prolonged calcination time, the carbon content in the samples gradually decreased, accompanied by a visible color lightening, resulting in reduced visible-light absorption. Compared to T-

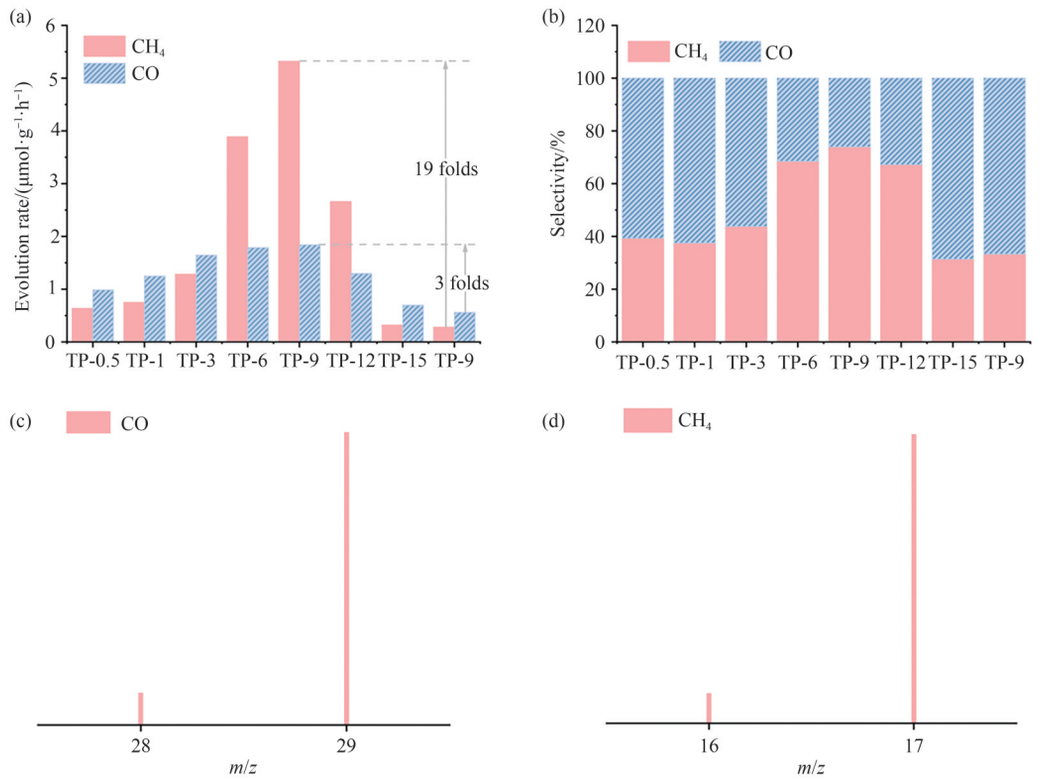

Comparison of (a) photocatalytic CO_2 reduction rates and (b) product selectivity of the samples; Mass spectra of (c) $^{13}CH_4$ and (d) ^{13}CO of TP-9

Fig. 6 Photocatalytic performance and selectivity of the samples for CO_2 reduction

图6 样品的光催化CO_2还原性能和产物选择性表征

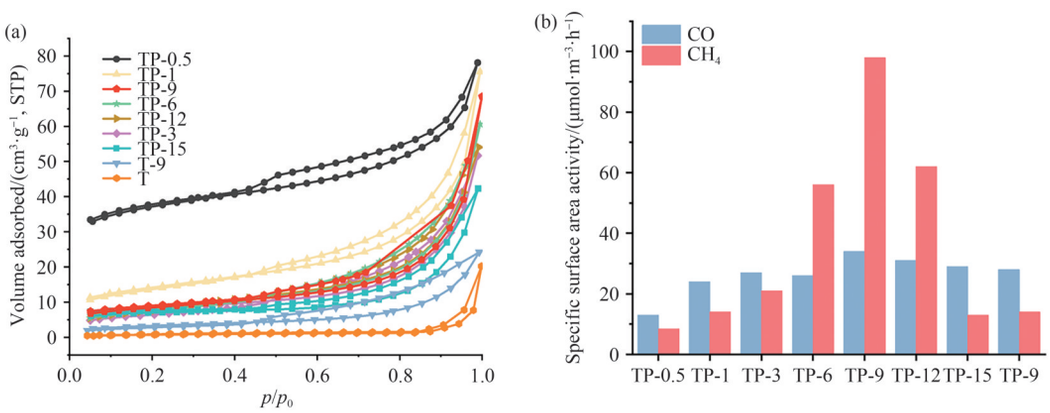

(a) N_2 adsorption-desorption isotherms; (b) Photocatalytic CO_2 reduction specific surface activity of the samples

Fig. 7 Specific surface area characterization of the samples

图7 样品的比表面积表征

9, the TP-9 sample exhibited lower carbon content and consequently weaker light-shielding effects, which ultimately enhanced its photocatalytic performance. However, since the oxidation of Ti_3C_2 only forms anatase TiO_2, the absorption edges of all calcined samples are consistent, suggesting that the increase in calcination time has a minimal impact on the band structure of the catalysts. Fig. 8b presented the Tauc plot curves of the samples. The band gaps of T-9 and TP-9 were 3.1 eV and 3.2 eV, respectively, which were close to that of the TiO_2 sample. This indicates that the band gap structure is not the determining factor for the photocatalytic CO_2 reduction performance.

The transfer and separation abilities of photogenerated carriers in the samples were characterized through photocurrent and impedance measurements. As shown in Fig. 9 (a), the TP-9 sample exhibited the strongest photocurrent response intensity, followed by TP-0.5, TP-1, TP-15, and

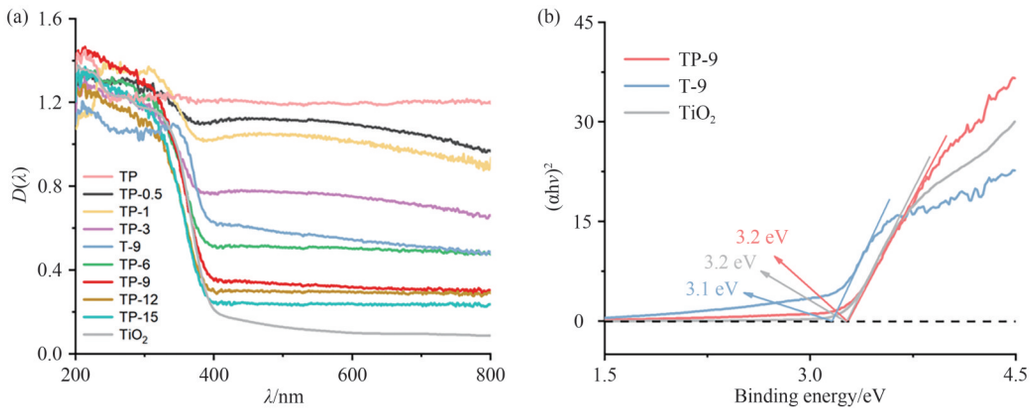

（a）UV-visible diffuse reflectance spectra；（b）Tauc plots of the samples

Fig. 8　Optical absorption characterization of the samples

图8　样品的光吸收性能表征

T-9，whichwas consistent with the order of photocatalytic performance of the samples. Conversely，the order of impedance magnitudes shown in Fig. 9（b）was opposite to that of the photocatalytic performance. This result indicates that the TP-9 sample has the best photogenerated carrier separation performance，which endows it with the best photocatalytic CO_2 reduction efficiency.

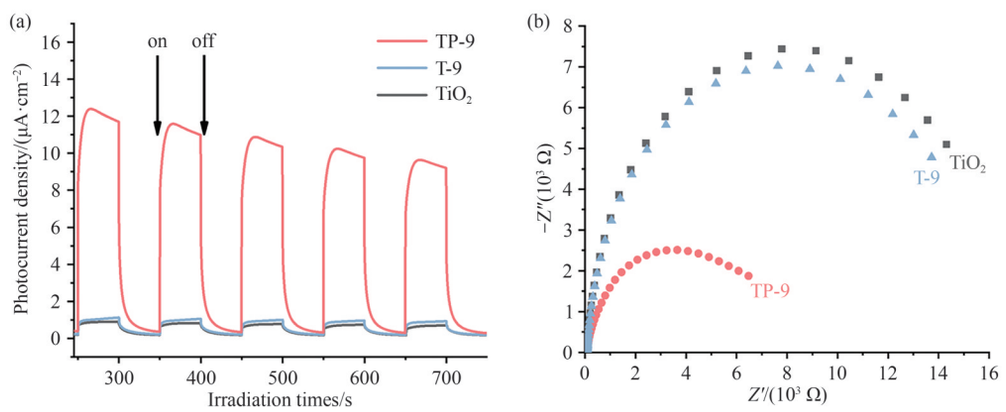

（a）Photocurrent curves；（b）Impedance plots of the samples

Fig. 9　Photoelectronic property characterization of the samples

图9　样品的光电性能表征

To investigate the CO_2 adsorption capabilities of the T-9 and TP-9 samples，a semi-quantitative method was employed to study their dark adsorption processes using *In situ* Diffuse Reflectance Infrared Fourier Transform Spectroscopy（DRIFTS）. As shown in Fig. 10，after 20 minutes of CO_2 adsorption，the peak intensities in T-9（Fig. 10(a)）were significantly lower than those in TP-9（Fig. 10b），indicating that TP-9 had a much stronger CO_2 adsorption ability. Specifically，the CO_2 adsorption amount on TP-9 reached the same level as T-9 after only 10 minutes，which was half the time required for T-9 to achieve the same adsorption amount after 20 minutes. This finding confirms that the bowl-like morphology of TP-9 facilitates CO_2 adsorption，which is always the key factor for CO_2 reduction performance.

To elucidate the photocatalytic CO_2 reduction mechanism of the TP-9 sample，*In situ* DRIFTS was employed to observe the functional group changes during the photocatalysis process. As illustrated in Fig. 11，upon light irradiation，the adsorbed CO_2 on the TP-9 sample reacted with photogenerated electrons to form *COOH. Subsequently，*COOH combined with H^+ to produce H_2O and CO. The CO further reacted with H^+ and electrons to form CH_3O*，which eventually converted to CH_4. The peak intensity of CH_3O* initially increased and then decreased，indicating its transformation into CH_4. The higher peak intensity of CH_3O* compared to COO^- also explains the higher selectivity of CH_4 in this sample. The specific mechanism

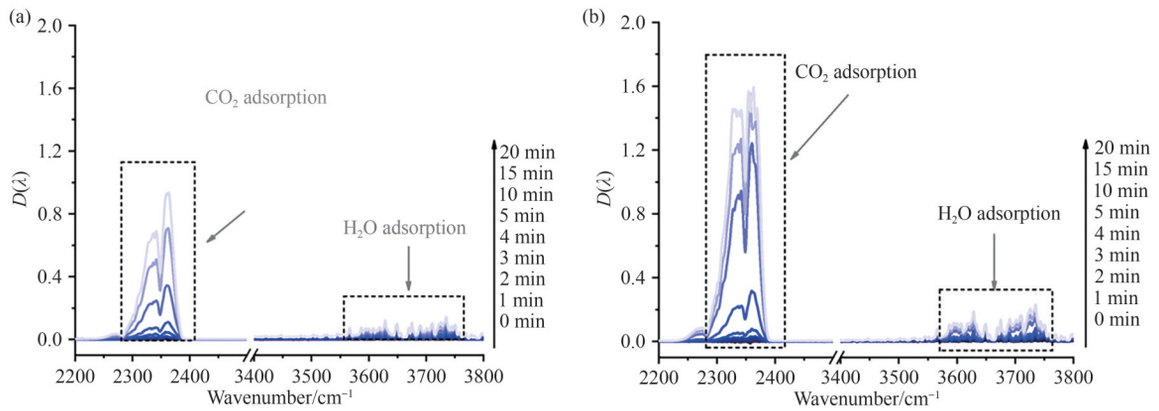

In situ DRIFTS curves for CO_2 and H_2O adsorption over (a) T-9 and (b) TP-9 in the dark state

Fig. 10 CO_2 adsorption performance of the samples

图 10 样品的CO_2吸附性能表征

is described by the following: $CO_2 \rightarrow *COOH \rightarrow *CO \rightarrow CO \rightarrow CO/*CHO \rightarrow CH_2O* \rightarrow CH_3O* \rightarrow CH_4$[42].

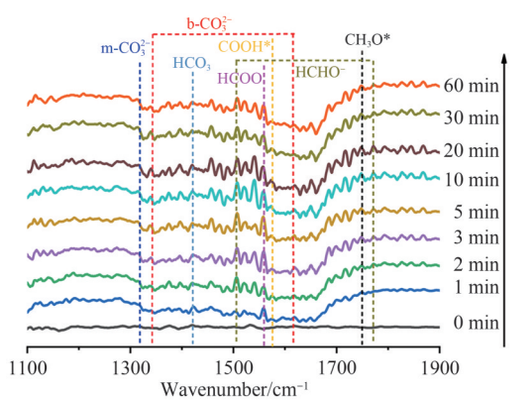

Fig. 11 *In situ* DRIFTS curves of the TP-9 under light irradiation

图 11 TP-9样品在光照下的原位DRIFTS曲线

Based on the experimental findings, a plausible mechanism has been elucidated to account for the photocatalytic reduction of CO_2 by the TiO_2/C composite catalyst, as depicted in Fig. 12. Upon light irradiation, TiO_2 is excited by light, prompting the electrons in the valence band to jump to the conduction band. This process generates a substantial quantity of electron-hole pairs. Owing to the exceptional conductivity of the carbon layer, a significant portion of the h^+ is transferred to the carbon layer. This transfer effectively suppresses the recombination of holes and electrons, thereby ensuring an adequate supply of electrons to participate in the CO_2 reduction reaction. Furthermore, the unique bowl-shaped structure significantly enhances the CO_2 adsorption capacity of the catalyst. This facilitates the reaction between CO_2 molecules and electrons to form CH_3O* intermediates, ultimately leading to the predominant production of CH_4 with trace amounts of CO.

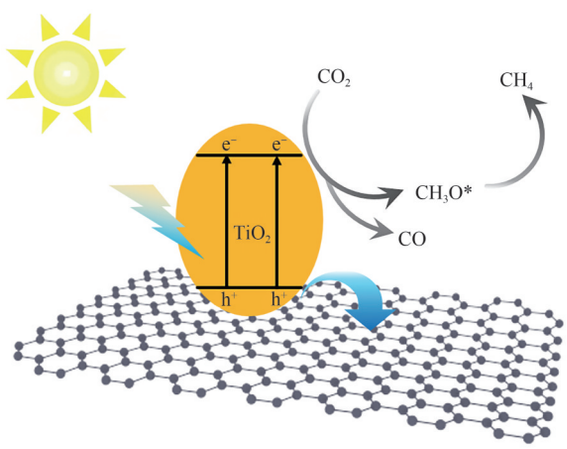

Fig. 12 Schematic diagram of photocatalytic CO_2 reduction mechanism

图 12 光催化CO_2还原机理图

3 Conclusion

In this study, PMMA was employed as a template to composite with Ti_3C_2 through electrostatic interactions, and then a calcination method was used to prepare bowl-like TiO_2/C composites. In these samples, the contact between TiO_2 and the C layer allows the photogenerated holes produced on the surface of TiO_2 to transfer to the C layer due to its high electrical conductivity. This transfer promotes the separation of photogenerated electron-hole pairs and induces more electrons to reduce CO_2. Moreover, the unique bowl-like morphology formed by calcining the PMMA-Ti_3C_2 composite not only provides a larger surface area but also facilitates the adsorption and activation of CO_2 molecules. The synergistic effects of the high conductivity of the C layer and the special morphology of the composite significantly improve the

photocatalytic CO_2 reduction performance and increase the selectivity for CH_4 production. This approach offers a promising solution for mitigating the environmental impact of CO_2.

Reference

[1] MURALI G, REDDY MODIGUNTA J K, PARK Y H, et al. A review on MXene synthesis, stability, and photocatalytic applications [J]. ACS Nano, 2022, 16(9): 13370-13429.

[2] LI Z, HUANG W, LIU J, et al. Embedding CdS@Au into ultrathin $Ti_{3-x}C_2T_y$ to build dual Schottky barriers for photocatalytic H_2 production [J]. ACS Catalysis, 2021, 11(14): 8510-8520.

[3] ZENG W, YE X, DONG Y, et al. MXene for photocatalysis and photothermal conversion: Synthesis, physicochemical properties, and applications [J]. Coordination Chemistry Reviews, 2024, 508: 215753.

[4] ZHAO W, SUN L, YANG L, et al. Highly efficient and selective photocatalytic CO_2 reduction to CO *via* molecular engineering of covalent organic framework [J]. Science China Materials, 2025, 68(1): 165-172.

[5] YAN T, WANG L, LIANG Y, et al. Polymorph selection towards photocatalytic gaseous CO_2 hydrogenation [J]. Nature Communications, 2019, 10(1): 2521.

[6] JIANG X, HUANG J, BI Z, et al. Plasmonic active "hot spots" -confined photocatalytic CO_2 reduction with high selectivity for CH_4 production [J]. Advanced Materials, 2022, 34(14): e2109330.

[7] JIA L, YANG L M, WANG W, et al. Preparation and characterization of Rb-doped TiO_2 powders for photocatalytic applications [J]. Rare Metals, 2024, 43(2): 555-561.

[8] 李恒超，王文广，吴梁鹏，等. 碳布负载多孔CdS纳米棒光催化剂的制备及其高效Cr(Ⅵ)还原光催化活性(英文) [J]. 中南民族大学学报(自然科学版)，2025, 44(1): 9-21.

[9] ZHANG J, ZHAO Y, QI K, et al. $CuInS_2$ quantum-dot-modified g-C_3N_4 S-scheme heterojunction photocatalyst for hydrogen production and tetracycline degradation [J]. Journal of Materials Science & Technology, 2024, 172: 145-155.

[10] LU L, ZHANG H, SUN Z, et al. Creation of robust oxygen vacancies in 2D ultrathin BiOBr nanosheets by irradiation through photocatalytic memory effect for enhanced CO_2 reduction [J]. Chemical Engineering Journal, 2023, 477: 146892.

[11] LAI K, SUN Y, LI N, et al. Photocatalytic CO_2-to-CH_4 conversion with ultrahigh selectivity of 95.93% on S-vacancy modulated spatial In_2S_3/In_2O_3 heterojunction [J]. Advanced Functional Materials, 2024, 34(49): 2409031.

[12] YUAN Z, ZHU X, GAO X, et al. Enhancing photocatalytic CO_2 reduction with TiO_2-based materials: Strategies, mechanisms, challenges, and perspectives [J]. Environmental Science and Ecotechnology, 2024, 20: 100368.

[13] YANG L, DU J, DENG J, et al. Defective Nb2C MXene cocatalyst on TiO_2 microsphere for enhanced photocatalytic CO_2 conversion to methane [J]. Small, 2024, 20(19): 2307007.

[14] HUANG K, LIANG G, SUN S, et al. Interface-induced charge transfer pathway switching of a Cu_2O-TiO_2 photocatalyst from p-n to S-scheme heterojunction for effective photocatalytic H_2 evolution [J]. Journal of Materials Science & Technology, 2024, 193: 98-106.

[15] LIU X, YANG W, YU C, et al. Influence of TiO_2 morphology on adsorption-photocatalytic efficiency of TiO_2-graphene composites for methylene blue degradation [J]. Journal of Environmental Chemical Engineering, 2018, 6(4): 4899-4907.

[16] LI H, ZHU B, CHENG B, et al. Single-atom Cu anchored on N-doped graphene/carbon nitride heterojunction for enhanced photocatalytic H_2O_2 production [J]. Journal of Materials Science & Technology, 2023, 161: 192-200.

[17] LI T, TSUBAKI N, JIN Z. S-scheme heterojunction in photocatalytic hydrogen production [J]. Journal of Materials Science & Technology, 2024, 169: 82-104.

[18] LI Y, DING L, YIN S, et al. Photocatalytic H_2 evolution on TiO_2 assembled with Ti_3C_2 MXene and metallic 1T-WS_2 as co-catalysts [J]. Nano-Micro Letters, 2019, 12(1): 6.

[19] TAHIR M, TAHIR B. Constructing S-scheme 2D/0D g-C_3N_4/TiO_2 NPs/MPs heterojunction with 2D-Ti_3AlC_2 MAX cocatalyst for photocatalytic CO_2 reduction to CO/CH_4 in fixed-bed and monolith photoreactors [J]. Journal of Materials Science & Technology, 2022, 106: 195-210.

[20] CAI X, WANG F, WANG R, et al. Synergism of surface strain and interfacial polarization on Pd@Au core–shell cocatalysts for highly efficient photocatalytic CO_2 reduction over TiO_2 [J]. Journal of Materials Chemistry A, 2020, 8(15): 7350-7359.

[21] ZHOU M, XUE S, FENG Q, et al. Carbon layers on Pt/TiO_2 induced dramatic promotion of photocatalytic H_2 production: A combined experimental and computation study [J]. Materials Today Energy, 2023, 34: 101294.

[22] LIU Y, XING M, ZHANG J. Ti^{3+} and carbon Co-doped TiO_2 with improved visible light photocatalytic activity [J]. Chinese Journal of Catalysis, 2014, 35(9): 1511-1519.

[23] JI L, ZHOU S, LIU X, et al. Synthesis of carbon- and

nitrogen-doped TiO_2/carbon composite fibers by a surface-hydrolyzed PAN fiber and their photocatalytic property [J]. Journal of Materials Science, 2020, 55(6): 2471-2481.

[24] WANG C, YANG K, WEI X, et al. One-pot solvothermal synthesis of carbon dots/Ag nanoparticles/TiO_2 nanocomposites with enhanced photocatalytic performance[J]. Ceramics International, 2018, 44(18): 22481-22488.

[25] ZHAO X, XIE W, DENG Z, et al. Salt templated synthesis of NiO/TiO_2 supported carbon nanosheets for photocatalytic hydrogen production [J]. Colloids and Surfaces A: Physicochemical and Engineering Aspects, 2020, 587: 124365.

[26] 高嵩, 赵薇芳, 蒋青青. 微波蚀刻制备超薄柔性MXenes及其纳米复合材料储钾机制[J]. 中南民族大学学报(自然科学版), 2025, 44(2): 153-161.

[27] CAO C, LI J, ZHANG L, et al. MXene-based 2D/2D Ti_3C_2/TiO_2 heterojunction with spatially separated redox sites for efficient photocatalytic N_2 reduction towards NH_3 [J]. Journal of Materials Science & Technology, 2025, 214: 180-193.

[28] HUANG H, SONG Y, LI N, et al. One-step *in situ* preparation of N-doped TiO_2@C derived from Ti_3C_2 MXene for enhanced visible-light driven photodegradation [J]. Applied Catalysis B: Environmental, 2019, 251: 154-161.

[29] HAN X, AN L, HU Y, et al. Ti_3C_2 MXene-derived carbon-doped TiO_2 coupled with g-C_3N_4 as the visible-light photocatalysts for photocatalytic H_2 generation[J]. Applied Catalysis B: Environmental, 2020, 265: 118539.

[30] LIU H, WU C, LV K, et al. *In-situ* generation of Au-carbon-TiO_2 Ohmic junction from Ti_3C_2 MXene for efficient photocatalytic H_2 evolution [J]. Journal of Materials Science & Technology, 2024, 188: 144-154.

[31] XIE H, HU L, WU F, et al. Self-templated synthesis of ultrathin nanosheets constructed TiO_2 hollow spheres with high electrochemical properties [J]. Advanced Science, 2016, 3(11): 1600162.

[32] ICHIJO T, SATO S, FUJITA M. Size-, mass-, and density-controlled preparation of TiO_2 nanoparticles in a spherical coordination template [J]. Journal of the American Chemical Society, 2013, 135(18): 6786-6789.

[33] DEKRAFFT K E, WANG C, LIN W. Metal-organic framework templated synthesis of Fe_2O_3/TiO_2 nanocomposite for hydrogen production [J]. Advanced Materials, 2012, 24(15): 2014-2018.

[34] ZHANG H, DONG F, FANG S, et al. Fabrication of macroporous titanium dioxide film using PMMA microspheres as template [J]. Journal of Colloid and Interface Science, 2012, 386(1): 73-79.

[35] WANG Y, WANG Y, YU L, et al. Enhanced catalytic activity of templated-double perovskite with 3D network structure for salicylic acid degradation under microwave irradiation: Insight into the catalytic mechanism [J]. Chemical Engineering Journal, 2019, 368: 115-128.

[36] ZHANG Y, RUAN K, ZHOU K, et al. Controlled distributed $Ti_3C_2T_x$ hollow microspheres on thermally conductive polyimide composite films for excellent electromagnetic interference shielding [J]. Advanced Materials, 2023, 35(16): 2211642.

[37] BI D, YI C, LUO J, et al. Polymer-templated nucleation and crystal growth of perovskite films for solar cells with efficiency greater than 21%[J]. Nature Energy, 2016, 1: 16142.

[38] WU C, HUANG W, LIU H, et al. Insight into synergistic effect of Ti_3C_2 MXene and MoS_2 on anti-photocorrosion and photocatalytic of CdS for hydrogen production [J]. Applied Catalysis B: Environmental, 2023, 330: 122653.

[39] TAN K, SAMYLINGAM L, ASLFATTAHI N, et al. Investigation of improved optical and conductivity properties of poly (methyl methacrylate) -MXenes (PMMA-MXenes) nanocomposite thin films for optoelectronic applications[J]. Open Chemistry, 2022, 20(1): 1416-1431.

[40] PENG C, ZHOU T, WEI P, et al. Regulation of the rutile/anatase TiO_2 phase junction *in situ* grown on-OH terminated $Ti_3C_2T_x$ (MXene) towards remarkably enhanced photocatalytic hydrogen evolution [J]. Chemical Engineering Journal, 2022, 439: 135685.

[41] LI H, SUN B, GAO T, et al. Ti_3C_2 MXene co-catalyst assembled with mesoporous TiO_2 for boosting photocatalytic activity of methyl orange degradation and hydrogen production[J]. Chinese Journal of Catalysis, 2022, 43(2): 461-471.

[42] LI J, LI K, TAN Q, et al. Facile preparation of highly active CO_2 reduction (001) TiO_2/$Ti_3C_2T_x$ photocatalyst from Ti_3AlC_2 with less fluorine [J]. Catalysts, 2022, 12(7): 785.

(责编&校对 刘钊)